Advanced Functional Materials

ADVANCED FUNCTIONAL MATERIALS
www.afm-journal.de

RESEARCH ARTICLE

Spiro-Configured Self-Assembling Molecule Modulates Phase Distribution at the Buried Interface for Efficient Sky-Blue Perovskite LEDs

Song Zheng[1] | Jihong Wu[2] | Zhibin Wang[1] | Kangqi Liao[1] | Zhehong Zhou[1] | Xin Zhou[1] | Longqi Lin[1] | Mingwei An[2] | Yang Wang[2] | Lingwei Zeng[3] | Ruidan Zhang[1] | Yongping Zheng[1] | Daqin Chen[1,4]

[1]College of Physics and Energy, Fujian Provincial Key Laboratory of Quantum Manipulation and New Energy Materials, Fujian Normal University, Fuzhou, P. R. China | [2]Strait Laboratory of Flexible Electronics (SLoFE), Fujian Key Laboratory of Flexible Electronics, Strait Institute of Flexible Electronics (SIFE, Future Technologies), Fujian Normal University, Fuzhou, Fujian, China | [3]School of Chemistry and Chemical Engineering, Hunan University of Science and Technology, Xiangtan, Hunan, P. R. China | [4]Fujian Provincial Engineering Technology Research Center of Solar Energy Conversion and Energy Storage, Fujian Normal University, Fuzhou, Fujian, P. R. China

Correspondence: Zhibin Wang (zhibinwang@fjnu.edu.cn) | Yang Wang (ifewangy@fjnu.edu.cn) | Daqin Chen (dqchen@fjnu.edu.cn)

Received: 8 May 2026 | **Revised:** 4 August 2026 | **Accepted:** 26 August 2026

Keywords: light-emitting diodes | perovskite | self-assembling molecule | sky blue | quasi-2D

ABSTRACT

Quasi-two-dimensional (quasi-2D) perovskites are promising candidates for efficient blue perovskite light-emitting diodes (PeLEDs), but their complex low-dimensional phase distributions often result in non-radiative recombination and emission broadening. Herein, we design 3-(4-(10H-spiro[acridine-9,9′-fluoren]-10-yl)phenyl)propanoic acid (SAF-PPA), a spiro-configured self-assembling molecule (SAM), to modify the hole-injection interface. The steric hindrance of SAF-PPA suppresses the disordered aggregation typically observed in linear SAMs, thereby promoting a more ordered interfacial structure. Moreover, the terminal carboxyl groups of SAF-PPA passivate uncoordinated Pb^{2+} defects and interact with organic spacer cations. This interaction reduces the accumulation of low-dimensional phases at the interface and promotes a more uniform vertical phase distribution. The SAF-PPA-modified films also exhibit reduced parasitic emission from minority phases and weaker exciton-phonon coupling. As a result, quasi-2D sky-blue PeLEDs achieve an external quantum efficiency of 21.9%, a turn-on voltage as low as 76% of the bandgap voltage, and an ultra-narrow electroluminescence linewidth of 15.4 nm. A representative SAF-PPA device further exhibits a T_{50} operational lifetime of 901.8 min under constant-current operation at an initial luminance of 500 cd m^{-2}. This work overcomes the long-standing efficiency-spectral purity trade-off in quasi-2D blue PeLEDs and provides a novel interfacial engineering strategy for high-performance optoelectronic devices.

1 | Introduction

The rapid advancement of high-quality displays and solid-state lighting has created a strong demand for luminescent materials that offer high color purity, low energy consumption, and low manufacturing cost. Metal halide perovskites have recently attracted broad interest for light-emitting diodes due to their outstanding luminescence, tunable bandgaps, high photoluminescence quantum yields (PLQY), and solution processability [1–7]. Nevertheless, the performance of blue perovskite

Song Zheng and Jihong Wu contributed equally to this work.

light-emitting diodes (PeLEDs) continues to lag behind that of red (>31%) [8] and green (>42%) [9] counterparts, presenting a major challenge for their use in full-color displays and lighting systems [10–14]. To improve the efficiency of blue PeLEDs, current strategies predominantly focus on bulk defect passivation or the use of conventional additives for interfacial modification to control crystallization [15–18]. Therefore, developing novel interfacial materials capable of spontaneously forming a compact and well-ordered interfacial layer—thus enabling uniform nucleation, phase-distribution regulation, and interfacial energetics optimization—is key to overcoming the bottleneck toward high-performance blue PeLEDs [19–21].

Self-assembling molecules (SAMs), typically comprising anchoring, spacer, and terminal groups, have emerged as promising interfacial modifiers because they can organize at surfaces and tune interfacial energy alignment [22–26]. On metal oxides, many conventional SAMs can form densely packed molecular layers. Carbazole phosphonic acid (CPA) derivatives play an increasingly vital role in enhancing PeLEDs, evolving from improving hole injection to a multifaceted strategy that regulates emissive layer conductivity, suppresses interfacial energetic disorder, and enhances thermodynamic stability. For instance, [4-(3,6-dimethyl-9H-carbazol-9-yl)butyl]phosphonic acid (Me-4PACz) deeply passivates undercoordinated lead defects via its electron-rich P═O bonds, facilitating hole injection while suppressing non-radiative recombination [27]. In our earlier work, blending hydrophobic Me-4PACz with hydrophilic polyvinyl pyrrolidone (PVP) as an underlying interlayer enabled green PeLEDs to achieve high brightness at ultralow voltage and extended operational lifetime [28]. Beyond interfacial roles, CPA molecules modulate electrical properties of the emissive layer; Di et al. used electron-withdrawing [4-(9H-carbazol-9-yl)butyl]phosphonic acid (4PACz) as a dopant to tune p-/n-type conduction while maintaining high PLQY [29]. Recently, Zhang et al. introduced [2-(9H-carbazol-9-yl)ethyl]phosphonic acid (2PACz) into a polymer hole transport layer, where π–π interactions promoted ordered chain stacking, suppressed energetic disorder, and improved charge transport [23, 30].

However, traditional linear or planar SAMs tend to aggregate excessively during spin-coating due to strong intermolecular interactions, leading to non-uniform molecular interlayers on substrates [31, 32]. This inhomogeneity limits full substrate coverage by the perovskite film and degrades PeLED performance. Recent studies show that breaking molecular planarity or introducing steric hindrance can reduce π--π stacking and improve interfacial uniformity. For example, Ding et al. first reported a spiro-type SAM 4PA-spiro (4-(10H-spiro[acridine-9,9′-fluorene]-10-yl)butylphosphonic acid), which features an orthogonal spiro[acridine-9,9′-fluorene] skeleton. Its twisted three-dimensional (3D) configuration increases intermolecular spacing and suppresses aggregation, yielding highly uniform substrate coverage [32]. Expanding on this, they further introduced heteroatoms (O, S) into a similar spiro skeleton. The resulting structure not only maintained anti-aggregation properties but also allowed lone-pair electrons from the heteroatoms to passivate Pb^{2+} defects, improving perovskite crystallinity [31]. These advances confirm that rational 3D spatial design, especially using spiro scaffolds, effectively mitigates interfacial aggregation and enables high-quality heterojunctions. Although spiro-configured SAMs have succeeded in perovskite solar cells, their application in PeLEDs remains largely unexplored.

In this work, we designed a novel spiro-configured SAM, named 3-(4-(10H-spiro[acridine-9,9′-fluoren]-10-yl)phenyl)propanoic acid (SAF-PPA), and introduced it for the first time into PeLEDs to modify the hole-injection interface. The rigid orthogonal spiro[acridine-fluorene] backbone at the molecular level forms strong π--π stacking with the underlying polymer while suppressing its intrinsic aggregation through steric hindrance, resulting in a highly dispersed and uniform interfacial network. A phenylpropyl linker occupies the central region, and a terminal carboxyl group (—COOH) is positioned at the top as a functional bridge. These exposed —COOH groups not only coordinate with under-coordinated Pb^{2+} ions at the buried perovskite interface but also interact with organic spacer cations. These interactions reduce the disordered aggregation of low-dimensional (low-n) phases at the bottom, phase heterogeneity, and parasitic radiative contributions from multiple low-n domains. The reduced phase heterogeneity is accompanied by a narrower emission spectrum, with an exceptionally narrow electroluminescence full width at half maximum (FWHM) of only 15.4 nm. Owing to these synergistic optimizations, the PLQY of SAF-PPA-modified sky-blue perovskite films increased from 43.6% to 85.4%. The corresponding PeLED devices achieved an external quantum efficiency (EQE) of 21.9% and a low turn-on voltage (V_{on}, at 1 cd m^{-2}) of 1.95 V, which is only 76% of the material's bandgap voltage (2.55 V). Under constant-current operation at an initial luminance of 500 cd m^{-2}, a representative SAF-PPA device further exhibited a T_{50} operational lifetime of 901.8 min.

2 | Results and Discussion

The molecular structure of the conventional SAM material 4PACz consists of a carbazole conjugated backbone connected to a flexible alkyl chain, exhibiting an overall planar configuration (Figure S1a,b). Although this configuration facilitates the dense packing of molecules on the substrate surface, the strong π–π interactions between the planar aromatic backbones tend to induce excessive molecular aggregation, thereby introducing morphological defects at the interface [33]. To overcome the above structural limitations, we designed and synthesized a novel SAM, SAF-PPA (Figure S1c,d). In terms of molecular design, SAF-PPA was rationally engineered for interfacial adaptation: a 3D orthogonal spiro[acridine-fluorene] aromatic backbone with significant steric hindrance is introduced at the bottom, aiming to bind with the underlying poly(N-vinylcarbazole) (PVK) via π–π stacking interactions; meanwhile, a phenyl propionic acid moiety is incorporated at the top, enabling the terminal carboxyl group (—COOH) to extend upward (Figure 1a). This highly non-coplanar steric configuration preserves favorable aromatic conjugation, while its steric hindrance effect suppresses the excessive self-aggregation of the molecules. Consequently, the packing morphology within the molecular layer is optimized (Figure 1b). More importantly, this specific molecular orientation positions the multifunctional carboxyl groups toward the perovskite layer, where they act as a critical interfacial bridge and passivation site between PVK and the perovskite. The synthetic route of SAF-PPA is presented in Figure S2, which involves a simple two-step

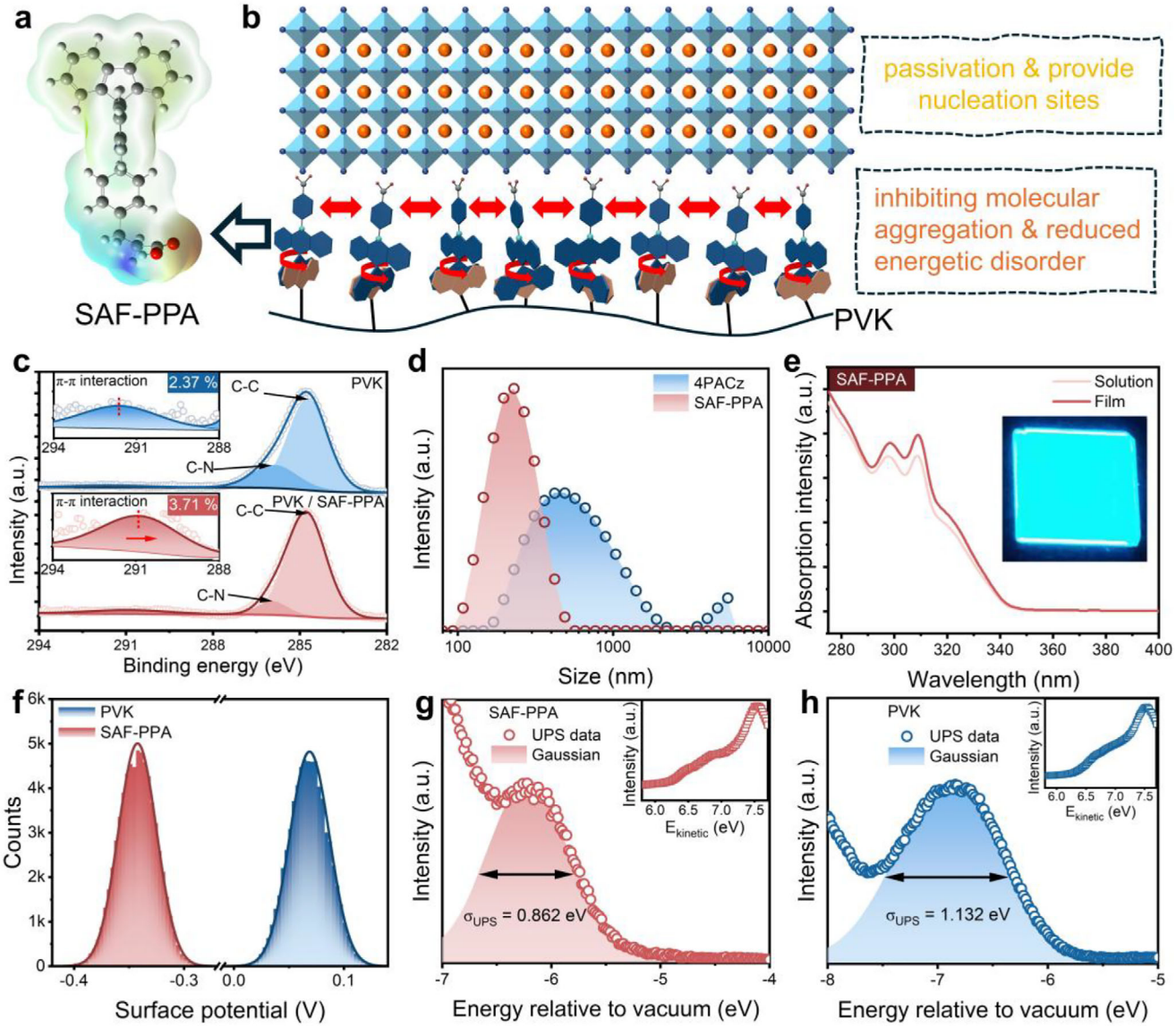

FIGURE 1 | (a) Electrostatic surface potential distribution of the SAF-PPA molecule. (b) Schematic diagram of the interlayer interaction mechanism among the SAM, PVK, and perovskite layers. (c) C 1s XPS spectra of the PVK and PVK/SAF-PPA films. The inset shows the satellite peak indicating π–π interactions. (d) DLS particle size distributions of 4PACz and SAF-PPA. (e) UV–vis absorption spectra of SAF-PPA in the solution and film states. The inset shows a photograph of the perovskite film spin-coated on the SAF-PPA substrate. (f) Statistical distributions of KPFM surface potentials for the PVK and SAF-PPA films. UPS valence band spectra and the Gaussian fitting curves at the high kinetic energy edges of the (g) SAF-PPA and (h) PVK films (the fitted width σ_{UPS} after subtracting the instrumental broadening is provided in the figure). The insets show the corresponding secondary electron cutoff edges.

reaction (i.e. C—N coupling and hydrolysis reactions) in a high total yield of 50%. To confirm the chemical structure of SAF-PPA, proton-1 and carbon-13 nuclear magnetic resonance (^{1}H NMR, ^{13}C NMR) as well as high-resolution mass spectrometry (HRMS) characterizations were performed (Figures S3–S5). The weak peak at a chemical shift of ~12 ppm is assigned to the active proton of the terminal carboxyl group; the multiplet resonance peaks in the range of 6.0–8.5 ppm correspond to the aromatic protons on the spiro backbone and benzene ring; and the signals in the range of 1.0–4.0 ppm originate from the alkyl chain protons connecting the aromatic ring and the carboxyl group [34]. The chemical shifts of the characteristic peaks for each component are highly consistent with the expected molecular structure.

To further investigate the interfacial coupling mechanism between SAF-PPA and the underlying PVK layer, X-ray photoelectron spectroscopy (XPS) characterizations were conducted. In the high-resolution C 1s spectra (Figure 1c), the pristine PVK film exhibits a characteristic satellite peak attributed to the π–π transition on the higher binding energy side of the main peak, accounting for an area fraction of 2.37%. Notably, upon the introduction of SAF-PPA, the relative area fraction of this π–π interaction peak increases significantly to 3.71%, accompanied by a distinct shift toward lower binding energy. This evolution of the interfacial electronic states verifies that the SAF-PPA molecules are stably physisorbed onto the carbazole-rich surface of PVK, predominantly through robust π–π stacking, and van der Waals forces [23, 35]. Benefiting from this strong non

-covalent interfacial coupling at the bottom, the outward-exposed —COOH at the top of SAF-PPA can serve as active functional sites to participate in the growth of the upper layer. They not only coordinate with the undercoordinated Pb^{2+} at the perovskite interface, thereby effectively passivating deep-level interfacial defects, but also act as uniform nucleation sites to regulate the crystallization kinetics, ultimately facilitating the formation of dense, and high-quality perovskite films. Electrostatic potential (ESP) distributions indicate that both SAF-PPA and 4PACz exhibit pronounced negative potentials at their polar anchoring ends (Figure S6a,b). However, frontier molecular orbital (FMO) analysis reveals fundamental differences in their electronic structures. Unlike the highly overlapped orbitals in 4PACz, the frontier orbitals of SAF-PPA are distinctly spatially separated due to its unique orthogonal spiro-configuration (Figure S6c–f): the highest occupied molecular orbital (HOMO) is predominantly localized on the electron-rich acridine unit, while the lowest unoccupied molecular orbital (LUMO) is concentrated on the opposite fluorene unit. This distinctive orbital separation not only effectively strengthens the intramolecular charge transfer dipole but also substantially facilitates interfacial hole injection and suppresses charge back-recombination [32, 36].

To assess how molecular structure influences aggregation, we first used dynamic light scattering (DLS) to examine solutions of the materials (Figure 1d). The planar molecule 4PACz shows a hydrodynamic radius primarily between 4000 and 6000 nm, confirming a strong tendency to agglomerate in solution. In contrast, the spiro-structured SAF-PPA exhibits a significantly narrower particle size distribution, centered between 100 and 300 nm, indicating much better dispersion [37]. We then turned to ultraviolet-visible (UV–vis) absorption spectroscopy to compare molecular stacking from solution to solid film. The 4PACz film shows a distinct redshift and peak broadening relative to its solution spectrum (Figure S7), signatures of aggregation driven by strong π- π stacking. The absorption profile of the SAF-PPA film, however, nearly overlaps with its solution spectrum (Figure 1e), showing no significant shift. This indicates that aggregation is effectively suppressed during film formation, which preserves a dispersed molecular state. To investigate whether the correlation between molecular structure and interfacial aggregation behavior extends beyond 4PACz to other interface materials, we selected five interfacial layers and systematically examined the quality of perovskite films deposited on them: the PVK reference, SAF-PPA, and three representative SAMs with distinct molecular architectures, namely short-linker 2PACz, long-linker 4PACz, and spiro-containing 4PA-spiro (Figure S8). Perovskite films deposited on the aggregation-prone 2PACz and 4PACz layers exhibit numerous pinholes, whereas those formed on PVK, 4PA-spiro, and SAF-PPA are continuous and pinhole-free. This broader comparison confirms that the sterically hindered spiro framework mitigates interfacial molecular aggregation, thereby promoting uniform perovskite film formation.

Atomic force microscopy (AFM) images provide direct morphological confirmation (Figure S9). The 4PACz film is rough, with visible aggregates and a root-mean-square (RMS) roughness of 1.09 nm. The SAF-PPA film is markedly smoother and more uniform, with an RMS roughness of 0.65 nm. These topographic observations align well with the aggregation behavior indicated by DLS and spectroscopy. The quality of this interfacial layer critically affects the perovskite deposited atop it. Due to severe underlying aggregation, a perovskite film spin-coated directly onto 4PACz shows dark spots and pinholes (Figure S7, inset). In contrast, the perovskite film grown on SAF-PPA is dense and continuous, exhibiting bright photoluminescence (Figure 1e, inset). Because pinholes promote current leakage and degrade device performance, 4PACz is not an ideal model for interface control. To evaluate the intrinsic benefits of SAF-PPA more clearly, we therefore use a pristine PVK film as the primary reference in the following optoelectronic analysis.

To understand how SAF-PPA influences the energy landscape of the PVK layer, we first examined the surface potential distribution using Kelvin probe force microscopy (KPFM). The reference PVK film shows a surface potential of 68.7 ± 18.1 mV (Figure 1f; Figure S10). After SAF-PPA modification, the potential shifts markedly downward to -342.5 ± 17.4 mV. Following calibration with a gold probe, the surface work functions (W_F) are determined as 4.41 eV for PVK and 4.13 eV for PVK/SAF-PPA. The reduced standard deviation points to a more uniform potential distribution, prompting a closer investigation of the interfacial electronic states. We therefore analyzed the valence band structure using ultraviolet photoelectron spectroscopy (UPS) (Figure 1g,h). In amorphous polymers, where band dispersion is minimal, the width of the lowest ionization energy peak (σ_{UPS}) reflects the intrinsic energetic disorder of the system. The unmodified PVK film exhibits a broad density of states, with $\sigma_{UPS} = 1.132$ eV. In contrast, σ_{UPS} narrows substantially to 0.862 eV for the PVK/SAF-PPA system. This pronounced spectral sharpening indicates that the SAF-PPA molecular interlayer homogenizes the interfacial electronic states, thereby reducing energetic disorder. A more uniform energy landscape can suppress energy dispersion in the amorphous network, facilitating faster hole transport and more efficient hole injection at the hole transport layer (HTL)/emissive layer (EML) interface [30, 38].

The properties of the underlying substrate critically influence both the film formation and the density of interfacial defects in the EML. We first measured the contact angle of the precursor solvent, dimethyl sulfoxide (DMSO), on each surface. The contact angle decreased from 38.5° on the reference substrate to 9.4° on the SAF-PPA-modified surface (Figure S11), indicating significantly enhanced wettability. This improvement lowers the energy barrier for heterogeneous nucleation, thermodynamically favoring the formation of a high-quality perovskite film. To directly visualize the film morphology (Figure 2a), we used scanning electron microscopy (SEM) to compare the top surfaces and the buried interfaces of the perovskite layers. While the top surfaces of both samples appear similar, their buried interfaces differ substantially. The interface of the film on the reference substrate is rough and contains visible pinholes (Figure 2b). X-ray diffraction (XRD) analysis further supports these findings. The diffraction peaks corresponding to the (100) and (200) crystal planes (at 15.3° and 30.8°) are significantly more intense for the perovskite film deposited on SAF-PPA (Figure 2c), demonstrating a marked improvement in overall film crystallinity.

This combined enhancement in interface quality and crystallinity stems primarily from the chemical interaction and growth modulation provided by the carboxyl groups in SAF-PPA.

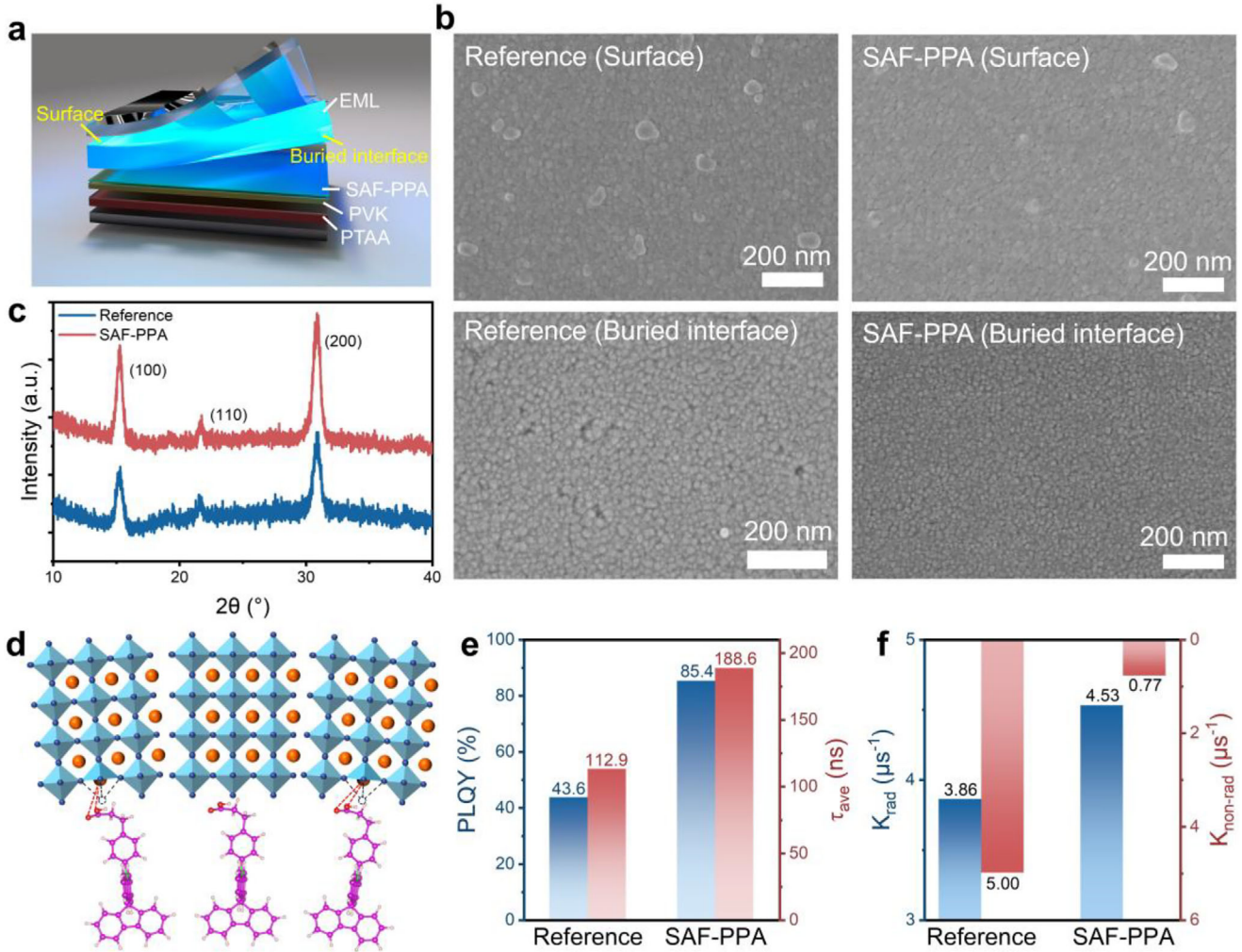

FIGURE 2 | (a) Schematic diagram of the surface and buried interface of the perovskite film. (b) SEM images of the surfaces and buried interfaces of the reference and SAF-PPA perovskite films. (c) XRD patterns of the perovskite films grown on the reference and SAF-PPA substrates. (d) Schematic diagram of the interaction mechanism between the —COOH group in the SAF-PPA molecule and the perovskite buried interface. (e) Statistical plots of the PLQY and τ_{ave} for the reference and SAF-PPA perovskite films. (f) Statistical plots of K_{rad} and $K_{non\text{-}rad}$ for the reference and SAF-PPA perovskite films.

These electron-rich groups can coordinate with under-coordinated Pb^{2+} ions at the bottom interface (Figure 2d). This interaction serves a dual purpose: it modulates the initial crystal growth kinetics to suppress void formation, and it simultaneously passivates defect sites at the buried interface.

To assess the resulting passivation effect, we performed steady-state photoluminescence (PL) and time-resolved photoluminescence (TRPL) measurements. The PLQY rises from 43.6% for the reference film to 85.4% for the SAF-PPA-modified film, while the average carrier lifetime (τ_{ave}) increases significantly from 112.9 to 188.6 ns (Figure S12; Figure 2e). Analysis of the recombination rates (Figure 2f) shows that the radiative recombination rate (K_{rad}) increases moderately to 4.53 μs^{-1} in the SAF-PPA system (Table S1). More strikingly, the non-radiative recombination rate ($K_{non\text{-}rad}$) drops sharply from 5.00 to 0.77 μs^{-1}, a substantial reduction. This pronounced suppression of non-radiative decay provides strong evidence that the density of defect states, particularly at the buried interface, has been effectively lowered [28, 39].

To understand the atomic-scale origin of this passivation effect, we used density functional theory (DFT) to model interactions between the substrate molecules and the perovskite surface. Charge density difference maps illustrate the interfacial charge transfer (Figure 3a; Figure S13a). Here, cyan regions indicate electron depletion and yellow regions indicate electron accumulation, clearly showing the orbital interactions involved. The calculations show that the adsorption energy (E_{ads}) of the PVK reference molecule on the perovskite surface is only −0.175 eV (Figure S13b,c). In contrast, the E_{ads} for the SAF-PPA system changes significantly to −0.536 eV, indicating that SAF-PPA forms a stronger adsorption interaction with uncoordinated ions at the interface [40]. Experimental evidence from ^1H NMR spectroscopy supports this finding. When $PbBr_2$ is added to SAF-PPA, the signal of the carboxyl proton peak at 12.2 ppm intensifies markedly (Figure S14), confirming that the carboxyl groups engage in strong coordination with Pb^{2+} [41].

We employed the space-charge-limited current (SCLC) model to quantify the defect density and carrier mobility of the films

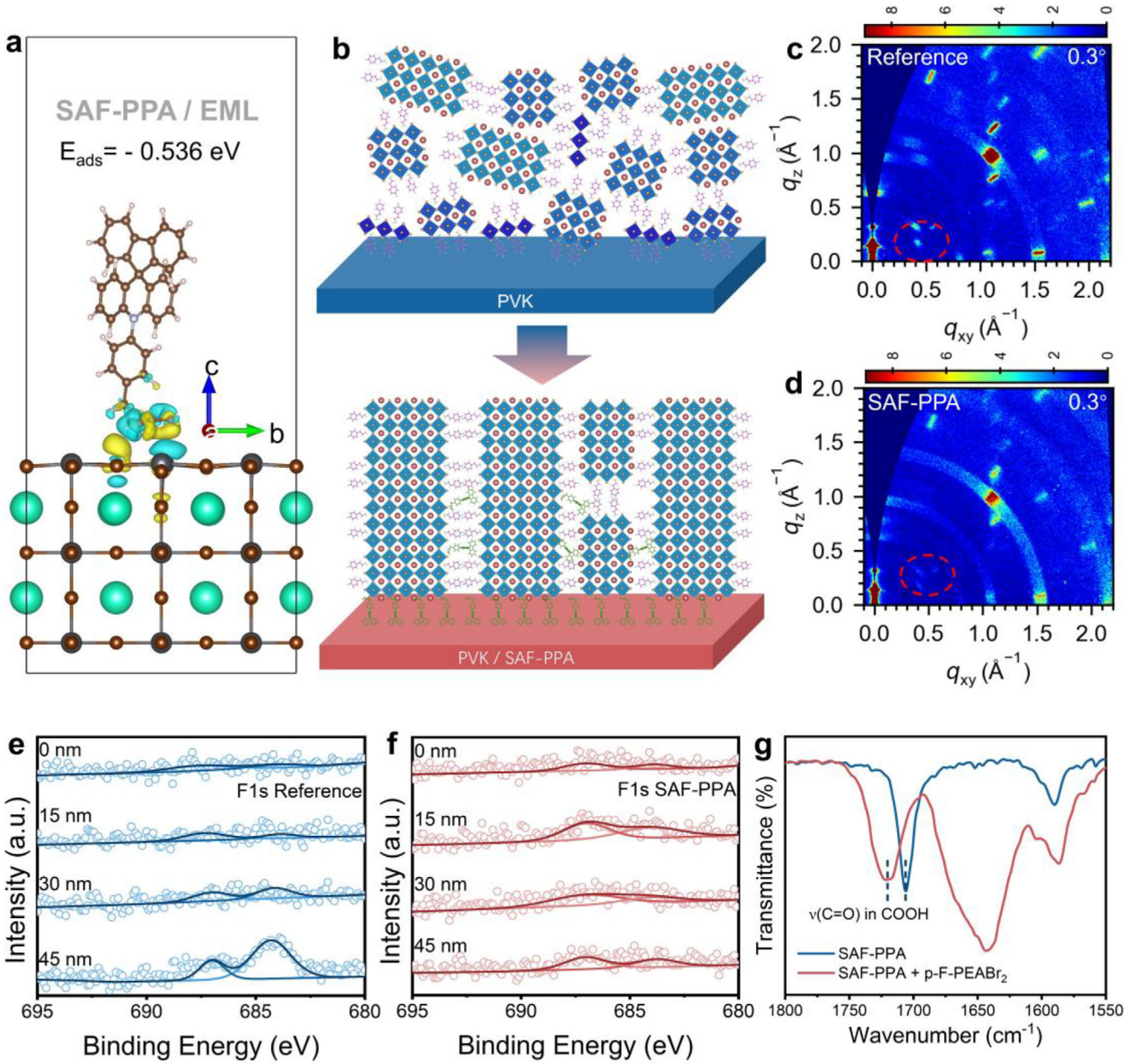

FIGURE 3 | (a) DFT-calculated charge density difference map and adsorption energy of the interaction between the $CsPbBr_3$ (001) surface and the SAF-PPA molecule. (b) Schematic diagram of the proposed vertical phase distributions in the reference and SAF-PPA perovskite films. GIWAXS patterns of the (c) reference and (d) SAF-PPA perovskite films at an incident angle of 0.3°. Depth-resolved F 1s XPS spectra of the (e) reference and (f) SAF-PPA perovskite films. (g) FTIR spectra of SAF-PPA and the mixture of SAF-PPA and p-F-PEABr.

(Figure S15). In hole-only devices (ITO/PTAA/PVK/EML/MoO_3/Ag), incorporating SAF-PPA lowers the trap-filled limit voltage from 1.11 to 0.69 V. This corresponds to a reduction in the hole trap density from 4.9×10^{16} to 3.0×10^{16} cm^{-3}, while the hole mobility increases from 8.9×10^{-5} to 1.7×10^{-4} cm^2 V^{-1} s^{-1}. The concurrent reduction in trap density and increase in carrier mobility confirm that SAF-PPA effectively suppresses charge loss at the bottom interface, thereby optimizing carrier injection, and recombination dynamics in the device.

Beyond interfacial morphology and defect distribution, the vertical phase arrangement within quasi-2D perovskite films critically influences interlayer charge transport. In a conventionally deposited film, low-n phases tend to aggregate disorderly near the bottom interface, leading to severe vertical phase inhomogeneity (Figure 3b). The introduction of SAF-PPA, however, reshapes this film formation, promoting a more uniform phase profile. Because SAF-PPA is directly exposed to the DMSO-based perovskite precursor during spin-coating, a fraction of the SAF-PPA molecules are likely solvated, and redistributed into the overlying emissive layer, while another fraction remains at the buried PVK/perovskite interface [39]. To probe the internal crystallization and phase distribution, we performed variable-angle grazing-incidence wide-angle X-ray scattering (GIWAXS) on 50 nm-thick perovskite films. At a shallow incident angle of 0.1° (probing depth ~10 nm), the two-dimensional GIWAXS patterns of the reference and SAF-PPA samples are very similar (Figure S16), indicating that the top surfaces of both films are dominated

by similar, well-crystallized high-n phases. When the incident angle is increased to 0.3° to probe the bulk region near the bottom interface (~40 nm depth), clear differences emerge [42]. The reference film shows distinct low-n diffraction spots in the low-q region (red circles, Figure 3c), whereas these signals are substantially attenuated in the SAF-PPA system (Figure 3d). At $q \approx 1.5$ Å^{-1}, the reference film shows intensity concentrated at specific azimuthal angles. In contrast, the more continuous Debye-Scherrer ring of the SAF-PPA film indicates a more random crystallite orientation. This broader azimuthal distribution spreads the scattering intensity over a wider angular range, potentially favoring more interconnected pathways for interdomain charge transport [43, 44]. Out-of-plane line profiles extracted from the 2D GIWAXS patterns provide quantitative evidence for the vertical phase distribution (Figure S17). The scattering features at $q \approx 0.43$ and 0.68 Å^{-1} are assigned to the (002) planes of the n = 2 and n = 1 phases, respectively [45]. These low-n features are pronounced in the reference film but substantially attenuated in the SAF-PPA film, indicating that SAF-PPA may suppress the preferential formation of low-dimensional phases near the buried interface.

Depth-resolved X-ray photoelectron spectroscopy (XPS) provides information on the vertical distribution of the fluorinated p-F-PEA$^+$ spacer (Figure 3e,f). For the reference film, the F 1s signal is weak at depths of 0–30 nm but becomes pronounced at 45 nm, indicating enrichment of p-F-PEA$^+$ near the buried interface. In contrast, the SAF-PPA film shows weak F 1s signals at all depths, supporting a more uniform distribution throughout the emissive layer. Room-temperature PL spectra collected from the surface and buried-interface sides provide additional optical verification (Figure S18). The surface spectrum of the reference film shows no distinct low-n emission, whereas its buried-interface spectrum exhibits additional features assigned to the n = 2 and n = 3 phases. By comparison, the surface and buried-interface spectra of the SAF-PPA film nearly overlap, with neither displaying discernible low-n emission. Together, these results support the proposed model of low-n phase accumulation at the bottom of the reference film and are consistent with reduced accumulation of low-n phases in the SAF-PPA film [16, 39, 46].

The combined spectroscopic and theoretical results suggest a possible molecular origin for this phase redistribution. FTIR spectroscopy reveals a distinct shift of the carboxyl-related vibration after mixing SAF-PPA with p-F-PEABr, indicating a specific interaction between the —COOH group of SAF-PPA and the organic spacer (Figure 3g). DFT calculations show that the optimized p-F-PEA/SAF-PPA complex adopts an N—H···O hydrogen-bonding configuration with an N···O separation of 3.1 Å and an adsorption energy of −0.23 eV (Figure S19a). In comparison, p-F-PEA remains separated from PVK by 3.9 Å and exhibits a much less negative adsorption energy of −0.09 eV (Figure S19b), indicating substantially weaker association. The shorter intermolecular distance and more favorable adsorption energy corroborate the FTIR results and provide a molecular basis for the stronger affinity of SAF-PPA toward the spacer [47]. This specific interaction regulates the distribution of p-F-PEA$^+$ during film formation, thereby mitigating its local accumulation and disfavoring the formation of low-n phases at the buried interface. The more uniform vertical phase distribution favors more continuous and efficient charge-transport pathways throughout the emissive layer.

To probe phase distribution and excited-state dynamics, we examined steady-state PL spectra at different temperatures. At 330 K, the PL profiles of both films are similar, dominated by the primary emission (Figure S20). Upon cooling to 90 K, however, suppressed thermal dissociation and reduced interlayer energy transfer reveal underlying phase segregation. The reference film shows three short-wavelength peaks at 428, 451, and 465 nm (Figure 4a), corresponding to low-n phases with n = 2, 3, and 4, respectively [48, 49]. In contrast, the SAF-PPA film maintains a single emission peak, with no detectable signals from low-n phases. We further employed ultrafast transient absorption (TA) spectroscopy to trace excited-state carrier dynamics. The reference film exhibits distinct ground-state bleaching (GSB) peaks near 432, 445, and 473 nm (Figure 4b), confirming the presence of multiple low-n phases [50, 51]. Moreover, its main GSB peak redshifts progressively with delay time, reflecting cascaded energy transfer from wide-gap low-n phases to narrower-gap high-n phases. The TA spectrum of the SAF-PPA film, by contrast, shows no GSB peaks from low-n phases, and its main GSB position remains nearly constant over time (Figure 4c). This indicates that excited carriers recombine radiatively within a uniform emissive phase, bypassing the non-radiative losses typically induced by low-n phase barriers [52, 53].

To quantify how crystallization affects exciton-phonon coupling, we analyzed temperature-dependent PL linewidths (Figure 4d,e). The FWHM vs. temperature was fitted using a Fröhlich longitudinal optical phonon broadening model (Figure 4f) [54]. The temperature-independent broadening term (Γ_0) decreases from 48.8 meV for the reference film to 39.9 meV for the SAF-PPA film, and the optical phonon coupling energy (E_{LO}) drops from 48.2 to 36.1 meV. Together with the reduced signals from low-n phases, this marked reduction in exciton-phonon coupling parameters is consistent with weaker defect-mediated exciton-phonon scattering in the SAF-PPA film.

To clarify the energy level alignment, we used UPS to determine the energy levels of PVK (Figure S21), SAF-PPA, and the EML, constructing a complete device energy level diagram (Figure 5a). Relative to the reference, SAF-PPA raises the interfacial HOMO level from −5.65 eV to a shallower −5.43 eV. Its LUMO level is −1.81 eV, which provides stronger electron-blocking capability compared with PVK (−2.15 eV). We fabricated reference devices (ITO/PTAA/PVK/EML/PO-T2T/LiF/Al) and target devices that include an optimized 0.5 mg ml^{-1} SAF-PPA interlayer (ITO/PTAA/PVK/SAF-PPA/EML/PO-T2T/LiF/Al) to compare their performance see Figure S22 for the concentration optimization process. The current-density-voltage (J–V) characteristics (Figure 5b) show that, before turn-on, the reference device exhibits substantial leakage current, attributable to pinholes and disordered low-n phases at the bottom perovskite interface. The SAF-PPA device reduces this leakage by about two orders of magnitude, confirming that the interlayer improves film morphology and passivates interfacial defects. Suppressed non-radiative recombination and enhanced carrier injection lead to markedly better electroluminescence. The V_{on} decreases from 2.35 V (92% of the band-gap voltage) for the

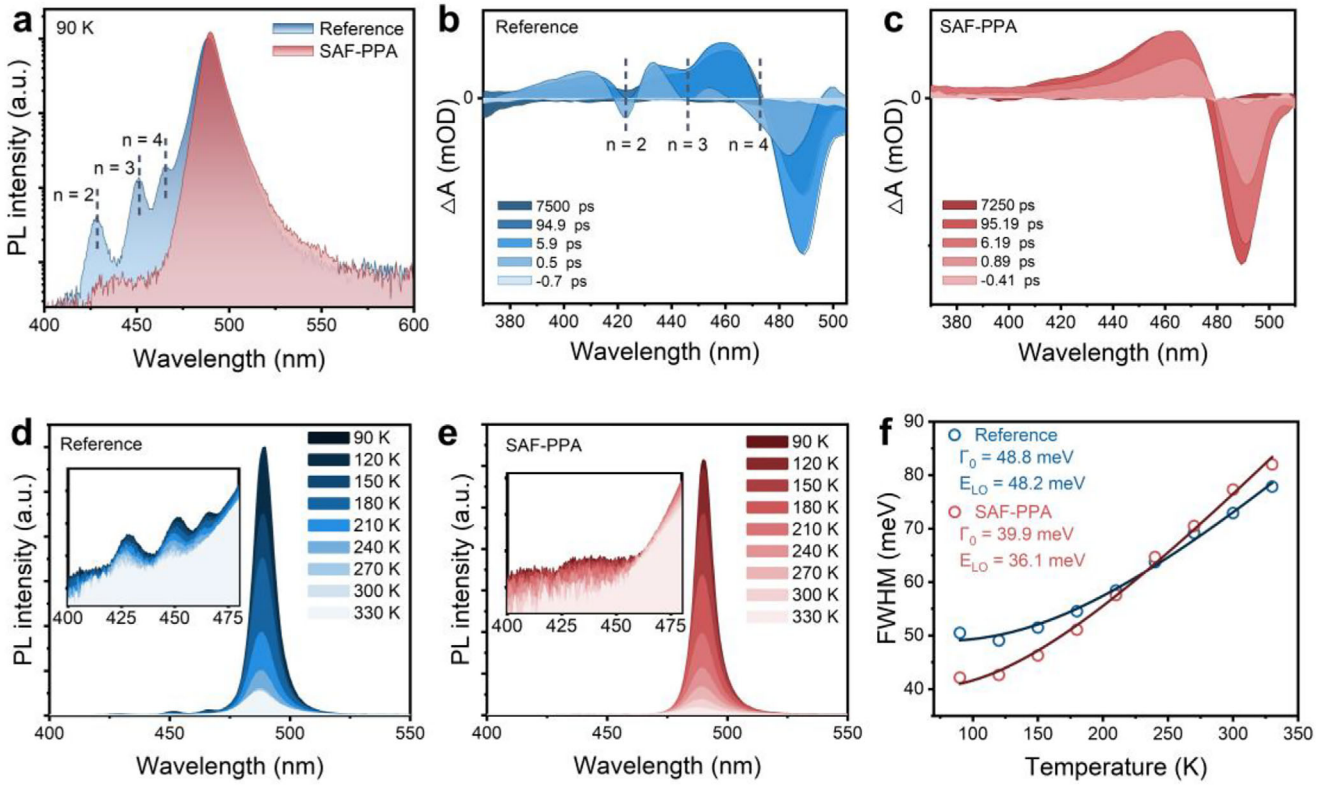

FIGURE 4 | (a) PL spectra of the reference and SAF-PPA perovskite films at 90 K. TA spectra of the (b) reference and (c) SAF-PPA perovskite films. Temperature-dependent (90–330 K) PL spectra of the (d) reference and (e) SAF-PPA perovskite films. The inset shows a magnified view of the low-dimensional phase emission region on a logarithmic scale. (f) Scatter plot and fitting curve of the FWHM of the PL emission peak for the perovskite films as a function of temperature.

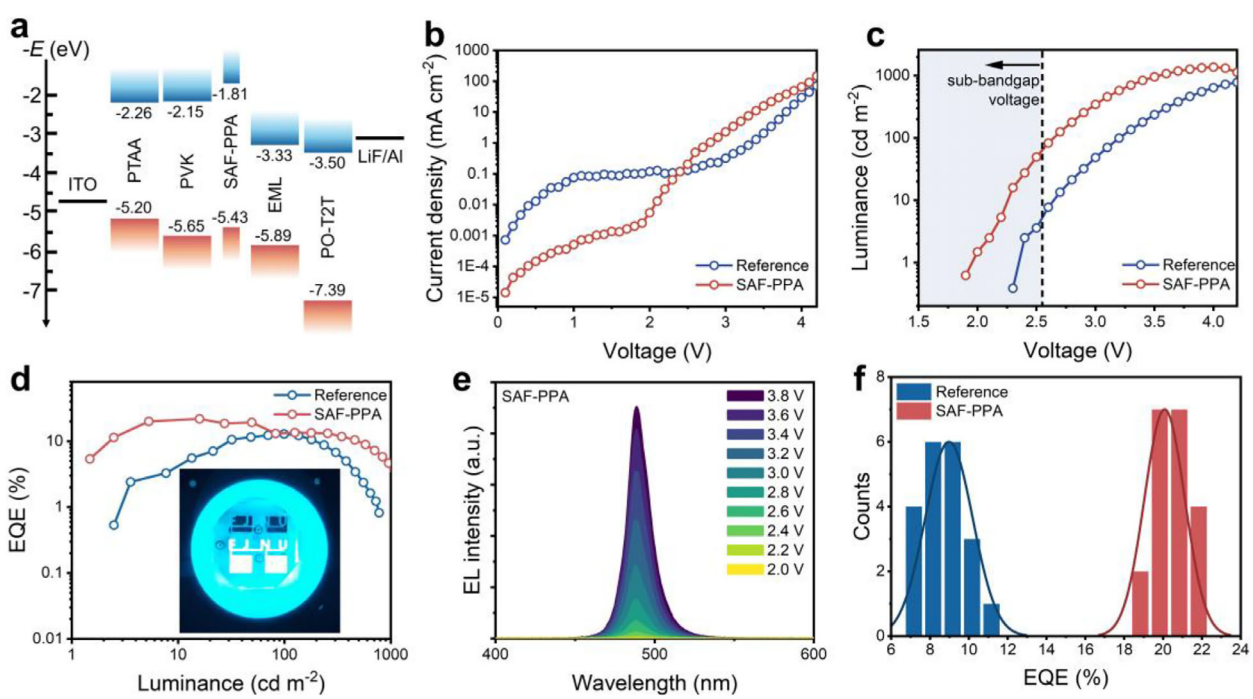

FIGURE 5 | (a) Schematic energy level diagram of the device. (b) *J*–*V* characteristics, (c) *L*–*V* characteristics (the shaded region represents the sub-bandgap voltage range), and (d) EQE–*L* characteristics of the reference and SAF-PPA devices (inset: photograph of the emitting device under operation). (e) EL spectra of the SAF-PPA devices under different driving voltages. (f) Statistical histograms of the EQE distribution for 20 individual devices each from the reference and SAF-PPA groups.

reference to 1.95 V (76% of the band-gap voltage) for the SAF-PPA device, achieving excellent sub-bandgap emission (Figure 5c). The maximum luminance of representative devices increases from 777.7 to 1371.3 cd m^{-2}, and the peak EQE rises from 12.8% to 21.9% (Figure 5d). The SAF-PPA device also exhibits superior spectral stability, with its electroluminescence peak remaining fixed at 488 nm under different driving voltages and a constant FWHM of 15.4 nm (Figure 5e). A broader comparison across representative interlayers further connects molecular structure and film integrity with device performance (Figures S23–S25). The elevated low-voltage currents of the 2PACz- and 4PACz-based devices are consistent with leakage through the pinholes; consequently, their peak EQEs are limited to 1.38% and 1.63%, with maximum brightness of 633.2 and 616.6 cd m^{-2}, respectively. In contrast, the more continuous film formed on 4PA-spiro enables a peak EQE of 14.2% and a maximum brightness of 946.5 cd m^{-2} (Figure S23). Voltage-dependent EL maps further reveal varying degrees of emission shift in the reference (PVK), 2PACz, 4PACz, and 4PA-spiro devices, while only the SAF-PPA device preserves a fixed emission, consistent with its more homogeneous quasi-2D phase distribution (Figure S24).

This distinction becomes more pronounced during continuous operation at an initial luminance of 500 cd m^{-2}: the T_{50} lifetimes of the reference, 2PACz, 4PACz, 4PA-spiro, and SAF-PPA devices are 0.82, 0.84, 4.0, and 67.4, and 901.8 min, respectively (Figure S25). The short lifetimes of the 2PACz and 4PACz devices are consistent with pinhole-mediated leakage, whereas the more than 13-fold lifetime advantage of SAF-PPA over 4PA-spiro likely reflects the combined benefits of its more rigid phenylene-containing linker and more homogeneous quasi-2D phase distribution, which help stabilize the buried interface under electrical stress. Compared with recently reported high-efficiency quasi-2D sky-blue PeLEDs, whose FWHMs typically exceed 20 nm (Figure S26), our device delivers one of the narrowest emission linewidths while maintaining a high EQE.

Performance statistics across 20 independently fabricated devices under each condition confirm the reproducibility of the approach (Figure 5f; Figure S27). The SAF-PPA devices yield an average EQE of 20.08% and an average maximum luminance of 1895.6 cd m^{-2}, with a narrow distribution. The corresponding averages for the reference devices are only 8.9% and 588.9 cd m^{-2}. These results demonstrate that SAF-PPA interfacial engineering reliably produces high-performance PeLEDs. This strategy successfully resolves the long-standing trade-off between efficiency and spectral purity in quasi-2D perovskites, offering an effective route to sky-blue PeLEDs with ultra-high color purity.

3 | Conclusion

In summary, we introduce an interfacial engineering strategy employing SAF-PPA, a self-assembling molecule with a rigid, and orthogonal spiro configuration. The steric hindrance of this molecule prevents the disordered aggregation commonly observed with conventional linear molecules, establishing a uniform hole-injection network. More importantly, the terminal carboxyl groups of SAF-PPA coordinate with under-coordinated Pb^{2+} ions and interact with organic spacer cations. This dual action is associated with reduced accumulation of low-n phases at the buried interface. The more uniform vertical phase profile may mitigate parasitic radiative and nonradiative recombination pathways associated with multi-phase coexistence and reduce exciton-phonon coupling. Consequently, the corresponding device achieves an EQE of 21.9%, a sub-bandgap V_{on} of 1.95 V, and an ultra-narrow electroluminescence linewidth with a FWHM of 15.4 nm. A representative SAF-PPA device also exhibits a T_{50} operational lifetime of 901.8 min under constant-current operation at an initial luminance of 500 cd m^{-2}. This work overcomes the persistent challenge in quasi-2D sky-blue PeLEDs, namely the trade-off between high efficiency and high color purity, and provides a new design paradigm for interfacial materials that feature both steric hindrance and multiple interactions.

Author Contributions

S.Z. and J.H.W. synthesized the materials, performed the main experiments, analyzed the data, and wrote the first draft. K.Q.L., Z.H.Z., X.Z., and L.Q.L. assisted with device fabrication, spectroscopic measurements, and data collection. L.W.Z. assisted with material characterization and data interpretation. R.D.Z. provided constructive suggestions for data analysis and assisted with sample characterization. Y.P.Z. assisted with the DFT calculations and related data analysis. Z.B.W., M.A., Y.W., and D.Q.C. conceptualized the idea, analyzed the experimental results, revised the manuscript, and supervised the project. All authors discussed the results and commented on the manuscript.

Acknowledgements

This research was supported by the National Natural Science Foundation of China (52102159, 52572155, 52272141, and 52573244), and the Natural Science Foundation of Fujian Province (2025J01655 and 2024J02014).

Conflicts of Interest

The authors declare no conflicts of interest.

Data Availability Statement

The data that support the findings of this study are available from the corresponding author upon reasonable request.

References

1. L. Kong, Y. Sun, B. Zhao, et al., "Fabrication of Red-Emitting Perovskite LEDs by Stabilizing Their Octahedral Structure," *Nature* 631 (2024): 73–79, https://doi.org/10.1038/s41586-024-07531-9.

2. T. W. Lee, "Over a Decade of Progress in Metal-Halide Perovskite Light-Emitting Diodes," *Advanced Materials* 37 (2025): 2508542, https://doi.org/10.1002/adma.202508542.

3. J. Qin, J. Zhang, X. Liu, et al., "Surfactant-Induced Hole Concentration Enhancement for Highly Efficient Perovskite Light-Emitting Diodes," *Nature Materials* 24 (2025): 778–784, https://doi.org/10.1038/s41563-025-02123-y.

4. R. Chen, Z. Wang, S. Zheng, et al., "Carbon Dots: Electroluminescent Devices for Lighting and Display Applications," *eScience* 6 (2026): 100517, https://doi.org/10.1016/j.esci.2025.100517.

5. C. Shen, H. Wang, X. Liang, et al., "Simultaneous Interfacial Modification and Crystallization Regulation for High-Performance Pure-Blue Quasi-2D Perovskite Light-Emitting Diodes," *ACS Energy Letters* 10 (2025): 3638–3646, https://doi.org/10.1021/acsenergylett.5c00695.

6. W. Bai, T. Xuan, H. Zhao, et al., "Perovskite Light-Emitting Diodes With an External Quantum Efficiency Exceeding 30%," *Advanced Materials* 35 (2023): 2302283, https://doi.org/10.1002/adma.202302283.

7. S. Zheng, Z. Wang, G. Zheng, et al., "Stable Sky-Blue Perovskite LEDs Achieved by Efficient Sub-Bandgap Emission With 24.5% PCE," *Advanced Functional Materials* 36 (2026): 21079, https://doi.org/10.1002/adfm.202521079.

8. S. Liu, D. Zhang, L. Wang, et al., "In-situ Formation of Oriented Perovskite Nanosheets With Tailored Optical Dipoles Enabling >30% EQE in Pure-Red LEDs," *Light: Science & Applications* 15 (2026): 163, https://doi.org/10.1038/s41377-026-02184-x.

9. J. Peng, X. Xue, S. Liu, et al., "Maximizing Perovskite Electroluminescence With Ordered 3D/2D Heterojunction," *Nature* 651 (2026): 76–82, https://doi.org/10.1038/s41586-026-10134-1.

10. Y. Yu, B.-F. Wang, Y. Shen, et al., "Efficient Blue Perovskite LEDs via Bottom-Up Charge Manipulation for Solution-Processed Active-Matrix Displays," *Advanced Materials* 37 (2025): 2503234, https://doi.org/10.1002/adma.202503234.

11. Y. Gao, Q. Cai, Y. He, et al., "Highly Efficient Blue Light-Emitting Diodes Based on Mixed-Halide Perovskites With Reduced Chlorine Defects," *Science Advances* 10 (2024): ado5645, https://doi.org/10.1126/sciadv.ado5645.

12. X. Zhang, Z. Liu, L. Wang, et al., "Manipulating Charge Transfer Dynamics and Stabilizing Lead Bromide Octahedra for Efficient Blue Perovskite Light-Emitting Diodes," *Nature Communications* 17 (2026): 1610, https://doi.org/10.1038/s41467-026-68315-5.

13. Y. Xia, C. Zou, Y.-H. Lou, et al., "Screening Fluorination Additives for Efficient Perovskite Light-Emitting Diodes," *Advanced Materials* 37 (2025): 2411231, https://doi.org/10.1002/adma.202411231.

14. Y. Xia, J.-C. Li, Z. Zhang, et al., "Spatial Crystallization Homogenization Boosts Scalable Perovskite Light-Emitting Diodes," *Advanced Materials* 37 (2025): 06413, https://doi.org/10.1002/adma.202506413.

15. S. Yuan, L. Dai, Y. Sun, et al., "Efficient Blue Electroluminescence From Reduced-Dimensional Perovskites," *Nature Photonics* 18 (2024): 425–431, https://doi.org/10.1038/s41566-024-01382-6.

16. Z. Chu, W. Zhang, J. Jiang, et al., "Blue Light-Emitting Diodes Based on Quasi-Two-Dimensional Perovskite With Efficient Charge Injection and Optimized Phase Distribution via an Alkali Metal Salt," *Nature Electronics* 6 (2023): 360–369, https://doi.org/10.1038/s41928-023-00955-7.

17. B. Chen, C. Peng, R. Guo, et al., "Dual-Function Self-Assembled Molecules as Hole-Transport Layers for Thermally Evaporated High-Efficiency Blue Perovskite Light-Emitting Diodes," *Advanced Materials* 37 (2025): 2411451, https://doi.org/10.1002/adma.202411451.

18. N. Jiang, Z. Wang, S. Zheng, et al., "All-Solution-Processed Sky-Blue Perovskite Electroluminescence Device via Integrated Supramolecular Host–Guest Post-Treatment," *Nano Letters* 26 (2026): 2735–2743, https://doi.org/10.1021/acs.nanolett.5c06313.

19. Y.-K. Wang, F. Jia, X. Li, et al., "Self-Assembled Monolayer–Based Blue Perovskite LEDs," *Science Advances* 9 (2023): adh2140, https://doi.org/10.1126/sciadv.adh2140.

20. J. Dong, B. Zhao, H. Ji, et al., "Multivalent-Effect Immobilization of Reduced-Dimensional Perovskites for Efficient and Spectrally Stable Deep-Blue Light-Emitting Diodes," *Nature Nanotechnology* 20 (2025): 507–514, https://doi.org/10.1038/s41565-024-01852-6.

21. K. Wei, M. Cui, C. Hu, et al., "Managing Edge States in Reduced-Dimensional Perovskites for Highly Efficient Deep-Blue LEDs," *Advanced Materials* 37 (2025): 2412041, https://doi.org/10.1002/adma.202412041.

22. S. Liu, J. Li, W. Xiao, et al., "Buried Interface Molecular Hybrid for Inverted Perovskite Solar Cells," *Nature* 632 (2024): 536–542, https://doi.org/10.1038/s41586-024-07723-3.

23. Z. Zhu, G. Zou, Y. Wang, et al., "Rational Molecular Design of Soluble Carbazole Phosphonic Acid for Hybrid Hole Transport Layers Enabling High-Efficiency Sky-Blue Perovskite LEDs," *Advanced Functional Materials* 35 (2025): 2500310, https://doi.org/10.1002/adfm.202500310.

24. Y. Zhong, Z. Fang, N. Ma, et al., "Suppressing Adsorption Disorder of Self-Assembled Molecules for Efficient Perovskite/Silicon Tandem Solar Cells," *Advanced Functional Materials* 36 (2026): 25359, https://doi.org/10.1002/adfm.202525359.

25. S. Zhang, X. Jiang, X. Wang, et al., "Complementary Self-Assembled Monolayers Enabling Improved Energy Level Alignment in Inverted Perovskite Solar Cells," *Journal of Energy Chemistry* 104 (2025): 136–145, https://doi.org/10.1016/j.jechem.2024.12.040.

26. X. Huang, T. Wang, W. Chen, et al., "Bottom-Up Regulation of Perovskite Growth and Energetics via Oligoether Functionalized Self-Assembling Molecules for High-Performance Solar Cells," *Angewandte Chemie International Edition* 64 (2025): 202507513, https://doi.org/10.1002/anie.202507513.

27. N. Li, Y. Xia, Y.-H. Lou, et al., "Dual-Functional Self-Assembled Molecule Enabling High-Performance Deep-Blue Perovskite Light-Emitting Diodes," *Advanced Functional Materials* 34 (2024): 2411227, https://doi.org/10.1002/adfm.202411227.

28. S. Zheng, Z. Wang, N. Jiang, et al., "Ultralow Voltage–Driven Efficient and Stable Perovskite Light-Emitting Diodes," *Science Advances* 10 (2024): adp8473, https://doi.org/10.1126/sciadv.adp8473.

29. W. Xiong, W. Tang, G. Zhang, et al., "Controllable p- and n-type Behaviours in Emissive Perovskite Semiconductors," *Nature* 633 (2024): 344–350, https://doi.org/10.1038/s41586-024-07792-4.

30. Z. Luo, W. Zheng, Y. Hua, et al., "Energetic Disorder Mitigation of Hole-Transport Layers via Molecular Assembly Boosts Charge Transport to Unlock Efficient and Stable Perovskite Light-Emitting Devices," *Nano Letters* 25 (2025): 17112–17121, https://doi.org/10.1021/acs.nanolett.5c04553.

31. B. Li, X. Liu, Y. Wei, et al., "High Performance Inverted Perovskite Solar Cells via Heteroatom-Containing Multifunctional Spiro Self-Assembled Monolayers," *Advanced Materials* 37 (2025): 00732, https://doi.org/10.1002/adma.202500732.

32. X. Zhang, B. Li, S. Zhang, et al., "A Spiro-type Self-Assembled Hole Transporting Monolayer for Highly Efficient and Stable Inverted Perovskite Solar Cells and Modules," *Energy & Environmental Science* 18 (2025): 468–477, https://doi.org/10.1039/d4ee01960a.

33. C. Shi, J. Wang, X. Lei, et al., "Modulating Competitive Adsorption of Hybrid Self-Assembled Molecules for Efficient Wide-Bandgap Perovskite Solar Cells and Tandems," *Nature Communications* 16 (2025): 3029, https://doi.org/10.1038/s41467-025-58111-y.

34. D. B. Stubing, S. Heng, and A. D. Abell, "Crowned Spiropyran Fluoroionophores With a Carboxyl Moiety for the Selective Detection of Lithium Ions," *Organic & Biomolecular Chemistry* 14 (2016): 3752–3757, https://doi.org/10.1039/c6ob00468g.

35. M. Gao, Z. Ou, C. Wang, et al., "Multifunctional Buried Molecule-Bridge for High-Performance Inverted Perovskite Solar Cells," *Advanced Materials* 38 (2026): 14273, https://doi.org/10.1002/adma.202514273.

36. S. Kuila, H. Miranda-Salinas, J. Eng, et al., "Rigid and Planar π-Conjugated Molecules Leading to Long-Lived Intramolecular Charge-Transfer States Exhibiting Thermally Activated Delayed Fluorescence," *Nature Communications* 15 (2024): 9611, https://doi.org/10.1038/s41467-024-53740-1.

37. X. Zhang, Y. Wang, K. Zhang, et al., "Reinforcing Coverage of Self-Assembled Monomolecular Layers for Inverted Perovskite Solar Cells With Efficiency of 25.70," *Angewandte Chemie International Edition* 64 (2025): 202423827, https://doi.org/10.1002/anie.202423827.

38. Y. Deng, F. Peng, Y. Lu, et al., "Solution-Processed Green and Blue Quantum-Dot Light-Emitting Diodes With Eliminated Charge Leakage," *Nature Photonics* 16 (2022): 505–511, https://doi.org/10.1038/s41566-022-00999-9.

39. X. Wu, Z. Wang, S. Zheng, et al., "Stabilizing the Buried Interface Phase for Perovskite LEDs With a Remarkable T90 Lifetime at 1000 nit,"

Nano Letters 25 (2025): 18158–18166, https://doi.org/10.1021/acs.nanolett.5c05743.

40. H. Huang, Z. Wang, S. Zheng, et al., "Efficient and Stable Flexible PeLEDs Enabled by Polymer Interfacial Permeation Engineering," *Laser & Photonics Reviews* 20 (2026): 02523, https://doi.org/10.1002/lpor.202502523.

41. C. Kuang, Z. Hu, Z. Yuan, et al., "Critical Role of Additive-Induced Molecular Interaction on the Operational Stability of Perovskite Light-Emitting Diodes," *Joule* 5 (2021): 618–630, https://doi.org/10.1016/j.joule.2021.01.003.

42. W. Zhou, S. Ham, H. B. Lee, et al., "Tuning Transition Dipole Moment Alignment via Bifunctional Ligands in Perovskite Nanocrystal Light-Emitting Diodes," *Advanced Materials* 38 (2026): 17210, https://doi.org/10.1002/adma.202517210.

43. J. S. Kim, H.-D. Lee, J. H. Jung, et al., "Kinetically-Controlled Intermediate-Direct-Pinning for Homogeneous Energy Landscapes in Quasi-Two-Dimensional Perovskites for Efficient and Narrow Blue Emission," *Nature Communications* 16 (2025): 9590, https://doi.org/10.1038/s41467-025-62863-y.

44. J. Du, M. Righetto, M. Choghaei, et al., "Odd–Even Cation Engineering of the Excitation Transport Anisotropy in Two-Dimensional Perovskite Films," *ACS Nano* 20 (2026): 15706–15715, https://doi.org/10.1021/acsnano.6c05301.

45. K. Datta, A. Caiazzo, M. A. Hope, et al., "Light-Induced Halide Segregation in 2D and Quasi-2D Mixed-Halide Perovskites," *ACS Energy Letters* 8 (2023): 1662–1670, https://doi.org/10.1021/acsenergylett.3c00160.

46. S. Wang, Z. Yu, J. Qin, et al., "Buried Interface Modification and Light Outcoupling Strategy for Efficient Blue Perovskite Light-Emitting Diodes," *Science Bulletin* 69 (2024): 2231–2240, https://doi.org/10.1016/j.scib.2024.05.028.

47. F. Zhang, Y. Yang, Y. Gao, et al., "High-Performance Blue Perovskite Light-Emitting Diodes Enabled by Synergistic Effect of Additives," *Nano Letters* 24 (2024): 1268–1276, https://doi.org/10.1021/acs.nanolett.3c04267.

48. S. Wang, Z. Yu, X.-F. Yang, et al., "Multifunctional Additives With Cation–π Interactions Enable High-Performance Blue Perovskite Light-Emitting Diodes," *ACS Energy Letters* 10 (2025): 1183–1191, https://doi.org/10.1021/acsenergylett.4c03551.

49. Y. Jiang, C. Qin, M. Cui, et al., "Spectra Stable Blue Perovskite Light-Emitting Diodes," *Nature Communications* 10 (2019): 1868, https://doi.org/10.1038/s41467-019-09794-7.

50. M. Yuan, L. N. Quan, R. Comin, et al., "Perovskite Energy Funnels for Efficient Light-Emitting Diodes," *Nature Nanotechnology* 11 (2016): 872–877, https://doi.org/10.1038/nnano.2016.110.

51. N. Wang, L. Cheng, R. Ge, et al., "Perovskite Light-Emitting Diodes Based on Solution-Processed Self-Organized Multiple Quantum Wells," *Nature Photonics* 10 (2016): 699–704, https://doi.org/10.1038/nphoton.2016.185.

52. C. Sun, Y. Jiang, M. Cui, et al., "High-Performance Large-Area Quasi-2D Perovskite Light-Emitting Diodes," *Nature Communications* 12 (2021): 2207, https://doi.org/10.1038/s41467-021-22529-x.

53. K. Wang, Z.-Y. Lin, Z. Zhang, et al., "Suppressing Phase Disproportionation in Quasi-2D Perovskite Light-Emitting Diodes," *Nature Communications* 14 (2023): 397, https://doi.org/10.1038/s41467-023-36118-7.

54. S. Rudin, T. L. Reinecke, and B. Segall, "Temperature-Dependent Exciton Linewidths in Semiconductors," *Physical Review B* 42 (1990): 11218–11231, https://doi.org/10.1103/physrevb.42.11218.

Supporting Information

Additional supporting information can be found online in the Supporting Information section.

Supporting File: adfm78157-sup-0001-SuppMat.docx.